JOURNAL OF MATERIALS SCIENCE 27 (1992) 4201–4207

Microstructures of titanium–aluminides produced by laser surface alloying

J. H. ABBOUD, D. R. F. WEST
Department of Materials, Imperial College of Science, Technology, and Medicine, Exhibition Road, London SW7 2BP, UK

The microstructures of Ti–Al layers (from 43–80 at %Al) produced by laser surface alloying of titanium substrate with a powder feed technique have been investigated. The laser processing parameters were; 1.8 kW laser power, 3 mm beam diameter, 7 mm s^{-1} traverse speed, and values of powder flow rates of aluminium ranging from 0.07–0.11 g s^{-1}. The microstructures were dendrites of α_2 and interdendritic regions of $\alpha_2 + \gamma$ in the Ti–43 at %Al alloy; dendrites of either α_2 or $\alpha_2 + \gamma$ with interdendritic γ in the Ti–50 at %Al alloy; dendrites of $\alpha_2 + \gamma$ with interdendritic γ in the Ti–55 at %Al alloy; single phase γ in the Ti–60 at %Al alloy and $TiAl_3$ dendrites and Al solid solution in the interdendritic regions in the Ti–80 at %Al alloy. The microstructures were fine and comparable to those produced by other methods of rapid solidification processing. The microstructures of the Ti–50 and Ti–55 at %Al alloys were in agreement with the existence of the peritectic reactions: $L + \beta \rightarrow \alpha$ and $L + \alpha \rightarrow \gamma$, in the Ti–Al system.

1. Introduction

Intermetallic compounds based on titanium, such as Ti_3Al, TiAl, and $TiAl_3$ have attractive properties for high temperature applications including good oxidation resistance, low density, and high modulus. However, the use of these aluminides in practice is limited by poor ductility and formability.

Recently, rapid solidification processing of titanium–aluminides has shown the possibility of obtaining fine structures with small scale segregation [1–4]. For example, Whang *et al.* [1] prepared foils of 40 μm thickness by a hammer and anvil quenching technique. The microstructural analysis showed a mixture of $\alpha_2 + \gamma$ in the range 49–56 at %Al, and single phase γ in the range 56–62 at %Al. The grain size was 2–3 μm as compared with 60 μm in the conventional alloy. The microhardness was 480 Hv at 56 at %Al and 350 Hv at 62 at %Al. Graves *et al.* [2] have carried out atomization of Ti–50 at %Al alloy using a rotating electrode process under a helium atmosphere. The microstructures were single phase α_2 in the finest powder and a mixture of $\alpha_2 + \gamma$ in most of the other powders. The proportion of α_2 compared to γ decreased as the particle size increased; at particle sizes larger than 60 μm, γ became the dominant phase, and this was attributed to the decrease in cooling rate with increase in particle size. Melt spinning of Ti–50 at %Al alloy was studied and the structures were compared with those obtained by atomization [3]. The results showed dendrites of α_2 and interdendritic γ; during annealing, the α_2 decomposed to a lath structure consisting of $\alpha_2 + \gamma$. Recently, Hall and Huang [4] have prepared Ti–Al alloys (from 46–70 at %Al) by melt spinning. The results indicate the formation of meta-stable phases in most of the ribbons studied. For example, single phase γ has been observed in Ti–60 and Ti–65 at %Al alloys with APBs in some grains; the interpretation was given that a combination of high Al content and high cooling rate resulted in the solidification of disordered fcc TiAl which then ordered to TiAl upon cooling.

A previous report by the authors on the use of a CW CO_2 laser and powder feed technique has shown the possibility of obtaining Ti–Al alloyed layers with a range of compositions [5]; the dimensions and the compositions of the alloyed zone were closely related to the processing parameters (eg. power, beam diameter, and aluminium powder flow rates). Microstructural features of some alloyed zones containing up to 36 at %Al have been recently investigated [6]. Martensitic structures with various morphologies were observed and APBs within the martensitic regions were also detected in the high aluminium content (Ti–23, Ti–30, and Ti–36 at %Al) alloys [6].

The results reported here cover further structural investigations on another set of alloyed layers with aluminium contents between 43 and 80 at %.

2. Experimental procedure

A 2 kW CO_2 laser and a powder feed technique with an effective argon shrouding device, were used to produce a series of Ti–Al alloyed layers. The experimental procedure and processing parameters were as described previously [5]. After laser processing the alloyed layers were sectioned transversely and metallographically prepared by grinding (from 120–1200 grit), polishing with alumina (from 5–0.5 μm), and etching

0022–2461

with a solution of 2% HF, 10% HNO_3, and 88% distilled water. Scanning electron microscopy (SEM) linked with an energy dispersive spectrometer (EDS) was used for structural and compositional analysis. Thin foils were prepared for transmission electron microscopy (TEM) and scanning transmission electron microscopy (STEM) by cutting a thin slice ~ 1 mm thick parallel to the surface of the laser alloyed zones. The slices were ground down mechanically to ~ 100 μm and discs of 3 mm diameter were obtained using a spark erosion machine. Electropolishing was carried out using a twin jet apparatus employing a solution containing 10% sulphuric acid in methanol at 18V and at a temperature of $-30\,^{\circ}C$. The areas examined were estimated to be at approximately mid-depth position of the alloyed zones.

Microhardness measurements, typically totally around 8, were made along the width and across the thickness and an average value of each alloyed layer was calculated.

3. Results

3.1. Composition and hardness

The compositions and the hardnesses of the alloyed layers studied are presented in Table 1. EDS X-ray analysis on each alloyed zone showed reasonable homogeneity (scatter within ∓ 1 at %Al). Analysis performed on two alloyed layers showed an oxygen content of ~ 2300 p.p.m. as compared with the value of ~ 1300 p.p.m. in the CP Ti used as the substrate.

TABLE I Compositions and hardnesses of Ti–Al alloyed layers, 1.8 kW, 3 mm, and 7 mm s^{-1}

Sample No.	Powder flow rate ($g\,s^{-1}$)	Average Al (at %)	Average $\sim$ Hv ∓ 10
1	0.071	43	525
2	0.073	50	480
3	0.076	55	450
4	0.083	60	300
5	0.11	80	350

3.2. Structure

3.2.1. Ti–43 at %Al

The microstructure of this alloyed layer as observed by optical microscopy showed a featureless planar zone with a sharp interface between the alloyed zone and the substrate (Fig. 1a). Epitaxial growth from the substrate was not detected and no martensitic structure was observed. SEM micrographs using backscattered electron imaging on a polished sample showed dendrites and interdendritic regions (Fig. 1b) with an average primary dendrite arm spacing of ~ 5 μm. EDS using SEM showed that the aluminium contents in the dendrites and in the interdendritic regions were 40 and 46 at %Al, respectively. TEM examination showed that the dendrites contained APBs of size ~ 50–100 nm and had a hcp crystal structure with superlattice reflections consistent with the α_2 (Ti_3Al) structure; the regions between the dendrites showed a lamellar structure consisting of a mixture of $\alpha_2 + \gamma$ (Fig. 1c). The γ phase was in the form of thin plates between α_2 with spacings less than 25 nm, and containing no APBs. STEM EDS X-ray microanalysis of the regions between the dendrites ($\alpha_2 + \gamma$ lamellae) showed an average aluminium content of 47 at %Al, while the composition ranged between 38–41 at %Al in the dendrites.

3.2.2. Ti–50 at %Al

The microstructure of the surface alloyed layer containing Ti–50 at %Al is shown in Fig. 2a. A planar

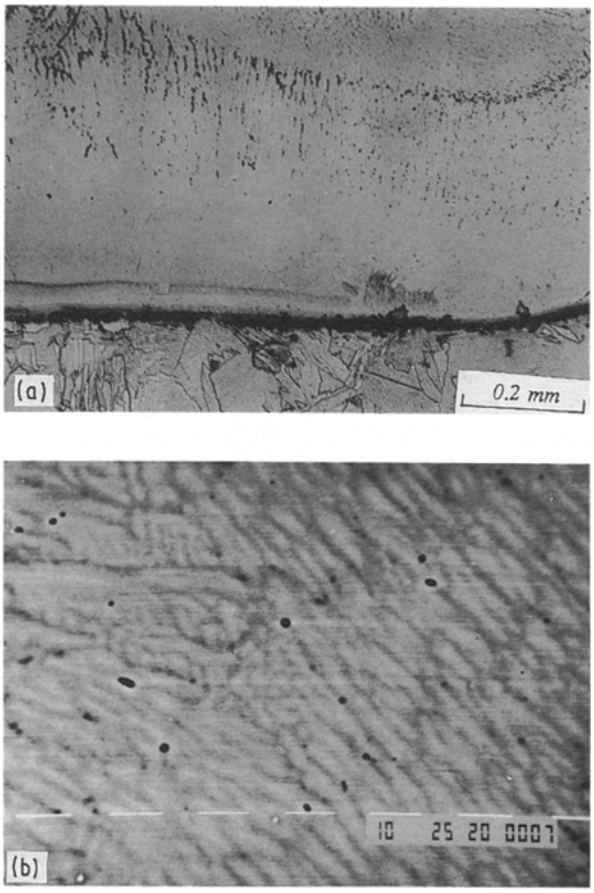

Figure 1 Ti–43 at %Al alloyed layer: (a) optical micrograph; (b) SEM–BSI micrograph; (c) TEM micrograph bright field showing dendrites α_2 and interdendritic $\alpha_2 + \gamma$.

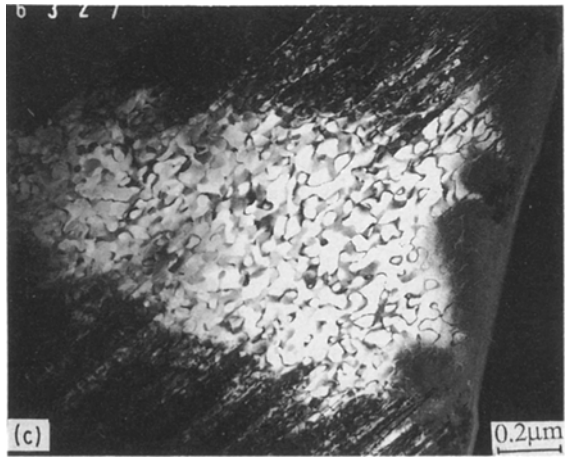

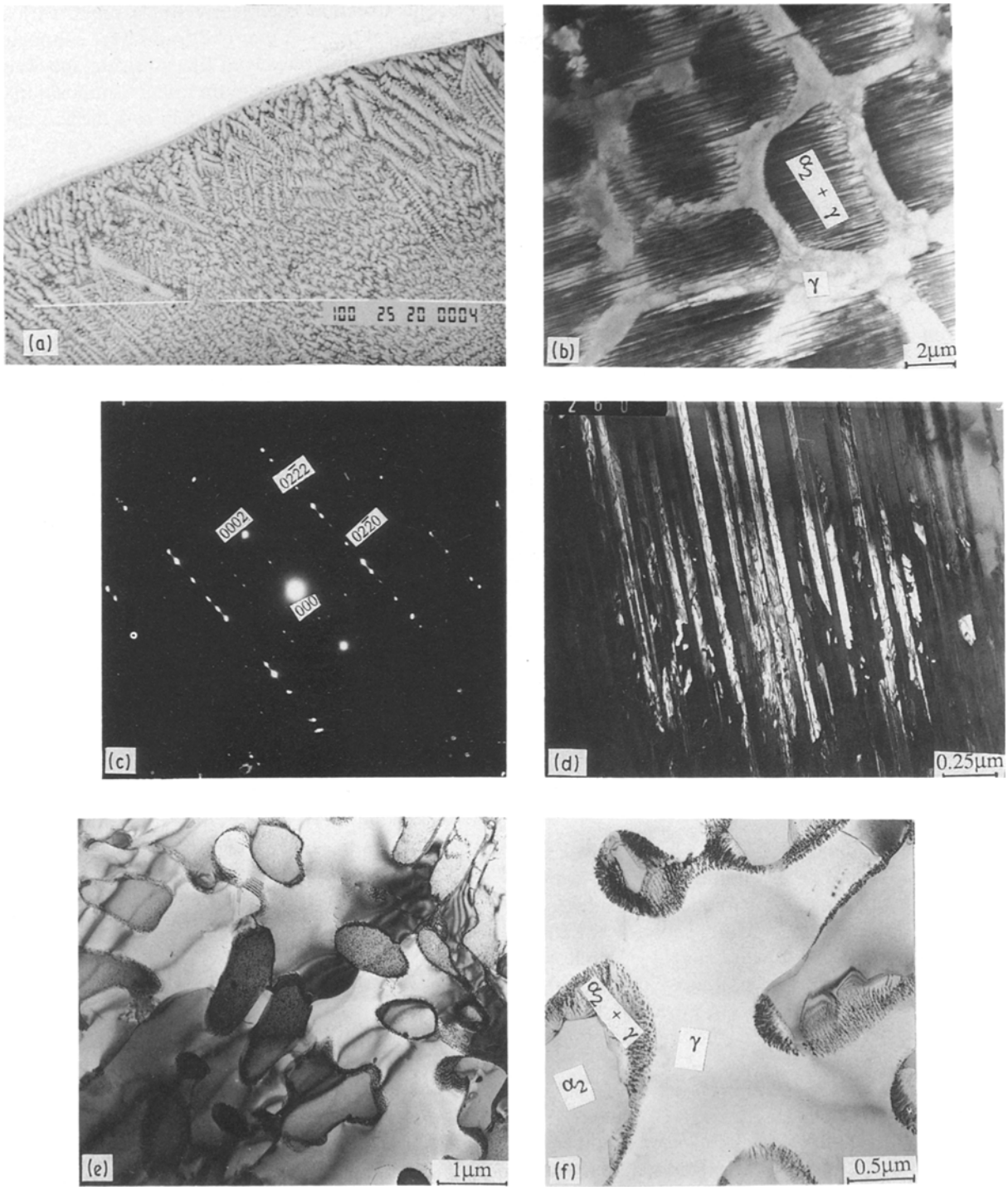

Figure 2 Ti–50 at %Al alloyed layer: (a) SEM–BSI micrograph; (b) TEM micrograph bright field showing dendrites $\alpha_2 + \gamma$ and interdendritic γ; (c) diffraction pattern taken from the dendrites, zone axis is $[0\,0\,0\,1]_{\alpha_2} // [1\,1\,1]_{\gamma}$ and $(2\,\bar{1}\,\bar{1}\,0)_{\alpha_2} // (1\,\bar{1}\,0)_{\gamma}$, ($\alpha_2$ reflections indexed); (d) TEM micrograph dark field using $(0\,1\,\bar{1}\,0)_{\alpha_2}$ reflection; (e) TEM micrograph bright field showing α_2 dendrites and interdendritic γ; (f) TEM micrograph bright field showing a mixture of $\alpha_2 + \gamma$ at the interface between α_2 and γ.

zone (featureless by optical microscopy) was seen at the interface between the alloyed zone and the heat affected zone changing to a dendritic structure away from the interface. Scanning electron microscopy using backscattered imaging showed that the extent of the planar zone ranged from 10–20 μm and the dendrites following the planar zone had an average primary spacing of 5 μm and an average secondary arm spacing of less than 2 μm. Compositional analysis carried out (using point analysis) on the primary dendrites, secondary dendrites, and interdendritic regions recorded values of 47.5, 49, and 53.5 at %Al, respectively; the average composition of an area 5 μm × 5 μm including the dendrites and interdendritic regions was 50 at %Al.

TEM analysis showed that some of the dendrites consisted of an $\alpha_2 + \gamma$ lamellar structure of spacings ranging from 10–50 nm (Fig. 2b) while the interdendritic regions consisted of γ phase. A selected area diffraction pattern (SADP) of an interdendritic region was indexed as f c t crystal structure while it showed a mixture of α_2 and γ in the dendrites. The diffraction

TABLE II EDS X-ray analyses of Ti–50 at %Al alloy on the bulk sample and on the thin foil, 1.8 kW, 3 mm, and 7 mm s^{-1}

Position	SEM Al (at %)	STEM Al (at %)
Primary dendrites ($\alpha_2 + \gamma$)	47.5	48
Secondary dendrites (α_2)	49	48.5
Interdendritic γ	53.5	53.8

pattern from the dendrites (Fig. 2c) showed that the α_2 and γ have the orientation relationship

$$[0\,0\,0\,1]_{\alpha_2} // [1\,1\,1]_{\gamma} \text{ and } (2\,\bar{1}\,\bar{1}\,0)_{\alpha_2} // (1\,\bar{1}\,0)_{\gamma}$$

This relationship has been found previously [7]. Dark field imaging using an α_2 reflection showed the presence of α_2 between the γ plates (Fig. 2d).

Other dendrites showed an α_2 structure containing APBs (Fig. 2e) and interdendritic regions consisting of γ; the interface between the dendrites and the interdendritic regions showed a mixture of α_2 and γ (Fig. 2f). STEM analysis showed similar average values of aluminium content in the dendrites which consisted of lamellar $\alpha_2 + \gamma$, and in the dendrites which showed α_2 only (Table II). The dendrites which contained only α_2 showed spacings of ~ 2 μm whereas the spacings of the dendrites with lamellar $\alpha_2 + \gamma$ were ~ 5 μm; the former are interpreted as secondary arms and the latter as primary dendrites.

3.2.3. Ti–55 at %Al

The microstructure of the Ti–55 at % Al alloy showed similar features to those observed in the Ti–50 at %Al alloy but with a smaller volume fraction of dendrites (Fig. 3a). TEM examination (Fig. 3b) showed that all the dendrites consisted of a mixture of $\alpha_2 + \gamma$ lamellae with interdendritic regions consisting of γ; a high density of dislocations was observed especially in the interface regions between the dendrites and γ regions.

3.2.4. Ti–60 at %Al

Fig. 4a presents a scanning electron micrograph taken from the central part of the Ti–60 at %Al alloyed zone. The structure was nearly single phase with a grain size of about ~ 5 μm. The grains were columnar adjacent to the interface with the substrate and were equiaxed in the remainder of the zone. Compositional analysis showed that the aluminium content was uniform in the grains with an average value of 60 at %Al corresponding to TiAl. X-ray diffraction showed many peaks which were indexed in agreement with the data from TiAl in the literature [8]. Examination by TEM showed dislocations in the γ grains (Fig. 4b) and thin layers identified by STEM analysis as $TiAl_3$ were occasionally observed between the γ grains (Fig. 4c). Electron diffraction patterns from the γ grains exhibited reflection spots in addition to the γ reflections. In general, the intensities of these extra reflections were weak (Fig. 4d) and dark field imaging using these reflections was not successful. The presence of extra reflections in Ti–60 at %Al alloy coexisting with the γ reflections has been reported before [4] and interpreted as due to the formation of a long period superlattice series.

3.2.5. Ti–80 at %Al

A typical structure of the Ti–80 at %Al alloyed layer as revealed by SEM is shown in Fig. 5a. Dendrites were observed with an average spacing of about 5 μm. SEM-EDS showed that the aluminium content was constant in the dendrites (74 ∓ 1 at %). X-ray diffraction showed that most of the peaks corresponded to $TiAl_3$ phase and to Al. TEM examination showed that the dendrites were $TiAl_3$ while the interdendritic regions contained a high density of dislocations. STEM analysis showed that the dendrites were $TiAl_3$ while the interdendritic regions were a solid solution of Al containing Ti up to 1.6 at %.

4. Discussion

4.1. Solidification front morphology

In the present Ti–Al alloyed layers, zones of featureless appearance adjacent to the unmelted substrate have been observed; such zones have been previously reported in a range of laser processed alloys, including

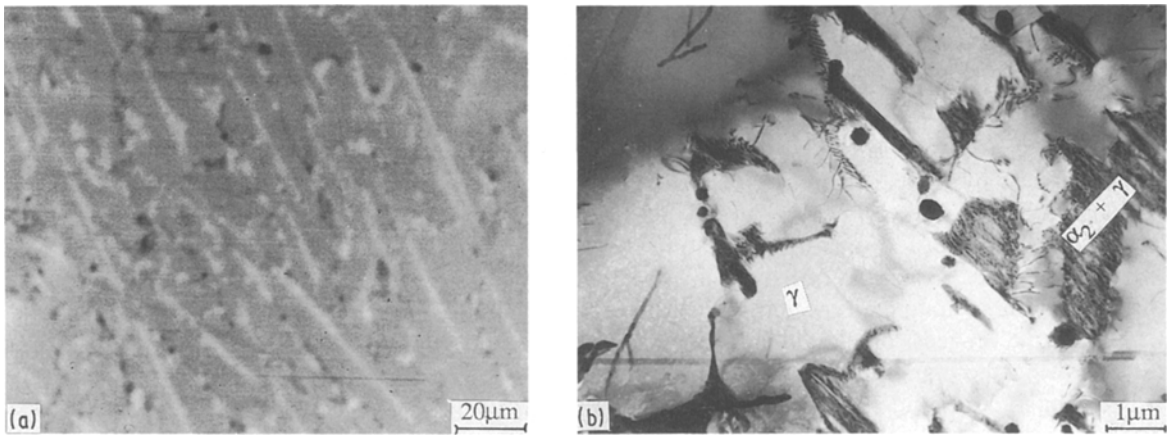

Figure 3 Ti–55 at %Al alloyed layer: (a) SEM–BSI micrograph; (b) TEM micrograph bright field showing $\alpha_2 + \gamma$ dendrites and interdendritic γ.

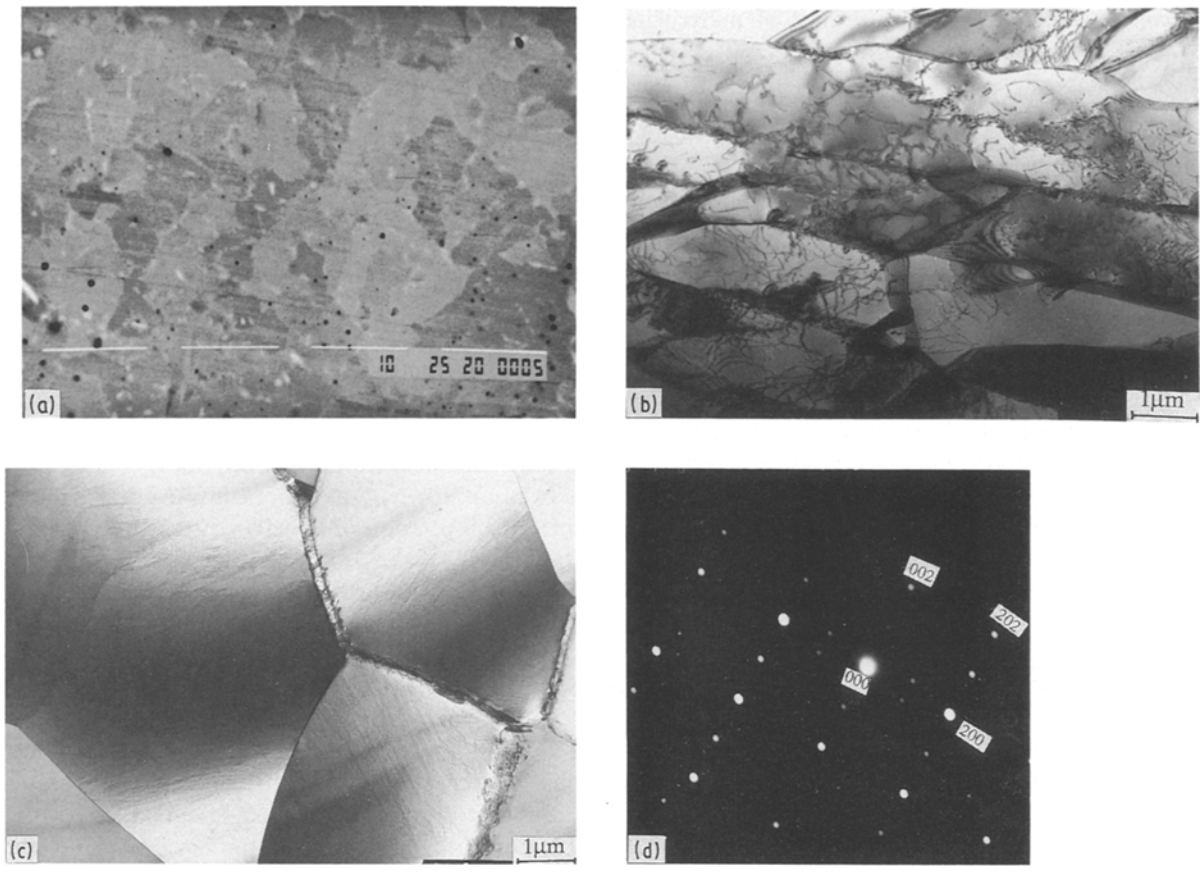

Figure 4 Ti–60 at %Al alloyed layer: (a) SEM–BSI micrograph; (b) and (c) TEM micrographs showing γ grains; (d) diffraction pattern of γ grain, zone axis is $(0\,\bar{1}\,0)\gamma$.

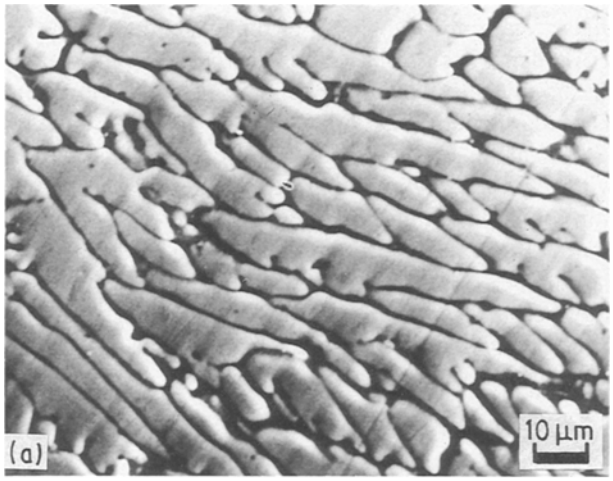

β-Ti alloys. These have been interpreted as the product of planar solidification due to high G/R ratios (G: temperature gradient, R: rate of solidification) in the laser melt pool, particularly at the beginning of freezing. With increasing distance from the substrate and with associated decrease in G/R ratio, cellular/dendritic solidification occurs. However, in work by the authors [6] on laser surface Ti–Al alloyed layers in the composition range 17–36 at %Al, these solidification modes were not metallographically observed, since

Figure 5 Ti–80 at %Al alloyed layer: (a) SEM–BSI micrograph; (b) TEM micrograph bright field showing $TiAl_3$ dendrites and interdendritic region; (c) TEM micrograph dark field using $(0\,0\,2)_{Al}$ showing dislocations in the interdendritic regions.

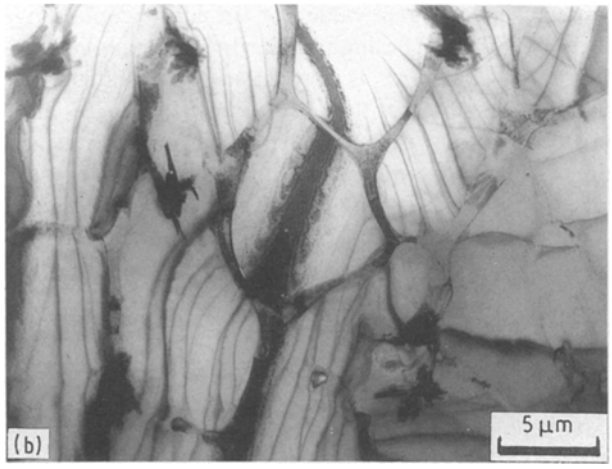

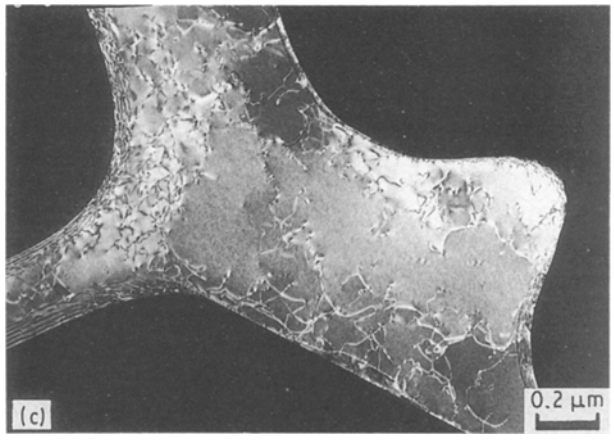

they were masked by the occurrence of martensite formation during solid state cooling.

4.2. Correlation of microstructures and phase diagram

The cooling rates achieved during solidification and in the solid state, which depend on alloyed zone dimensions, have not been calculated. However, on the basis of previous work on titanium alloys [5], the observation of dendrite arm spacings of $\sim 5\,\mu m$ in the Ti–43 at %Al alloyed zone indicates a cooling rate of the order of $\sim 10^3\,°C\,s^{-1}$ which is not enough to cause diffusionless solidification; therefore the microstructures can be interpreted on the basis of the binary Ti–Al phase diagram. The diagram as assessed by Murray [9] shows the peritectic reaction: $L + \beta \rightarrow \gamma$ at 1753 K, whereas the recent work of McCullough *et al.* [10] has shown the existence of two peritectic reactions: $L + \beta \rightarrow \alpha$ at ~ 1760 K and $L + \alpha \rightarrow \gamma$ at ~ 1740 K (Fig. 6); the latter work must be considered in relation to the alloy layers in the range 43–55 at %Al.

According to both the Murray and McCullough diagrams, the solidification of the Ti–43 at %Al alloy commences with β dendrites; at equilibrium at room temperature both diagrams show the composition to be in the $\alpha_2 + \gamma$ phase region. With rapid solidification cored β will form and according to the McCullough diagram, the peritectic reaction $L + \beta \rightarrow \alpha$ will occur, producing α containing ~ 47 at %Al which transforms to α_2 on cooling. The absence of γ in the original β dendrites indicates that the cooling rate is sufficiently rapid to prevent γ formation. However, the interdendritic regions were found to contain ~ 47 at %Al, the α having decomposed into $\alpha_2 + \gamma$. The structure could also be interpreted on the basis of the Murray diagram.

In the Ti–50 at %Al alloy, primary solidification should involve a small proportion of β dendrites according to the Murray diagram. The observed structure however showed a substantial proportion of dendrites (Fig. 2a) which is consistent with the McCullough diagram which predicts α as the primary phase. The interdendritic regions (found to be γ containing 53 at %Al) are consistent with the peritectic reaction $L + \alpha \rightarrow \gamma$ shown in the McCullough diagram. On rapid cooling the α transforms to $\alpha_2 + \gamma$ in the primary dendrites (~ 47.5 at %Al) while in the secondary dendrite arms containing ~ 49 at %Al, only α_2 is found, but with some decomposition to $\alpha_2 + \gamma$ at the dendrite/γ interfaces. It is not understood why γ precipitation from α is not observed in the secondary dendrites of higher Al content than the primary dendrites and thus providing greater supersaturation: the α_2/γ interfaces, however, provide sites for local formation of lamellar $\alpha_2 + \gamma$.

The Ti–55 at %Al alloy showed a smaller amount of primary dendrites which decomposed to form a lamellar $\alpha_2 + \gamma$ structure as in the primary dendrites of the Ti–50 at %Al alloy. The solidification and solid state cooling in the two alloys is therefore similar. The sequence, including the difference in the proportion of dendrites (α phase) is consistent with the McCullough phase diagram, but not with the Murray diagram.

Solidification of the Ti–60 at %Al alloy (Murray diagram) occurs to form primary γ grains and under equilibrium conditions the structure is single phase; however, with rapid cooling, enrichment of the liquid in aluminium leads to the $L + \gamma \rightarrow TiAl_3$ peritectic and to the observed intergranular layers of $TiAl_3$.

The Ti–80 at %Al alloy lies in the region of the phase diagram in which primary solidification of $TiAl_3$ dendrites is followed by the peritectic region of the liquid with $TiAl_3$ to produce Al (solid solution). The equilibrium solid solubility of Ti in Al is only ~ 0.05 at %, but Kerr *et al.* [11] have shown that with relatively high cooling rates, supersaturated aluminium solid solution nucleated above the peritectic temperature. In the present work, the STEM analysis value of ~ 1.6 at %Al in the interdendritic regions may be partly due to some dendrite areas rich in Ti being included in the analysis. However, the effect may be an indication of supersaturation.

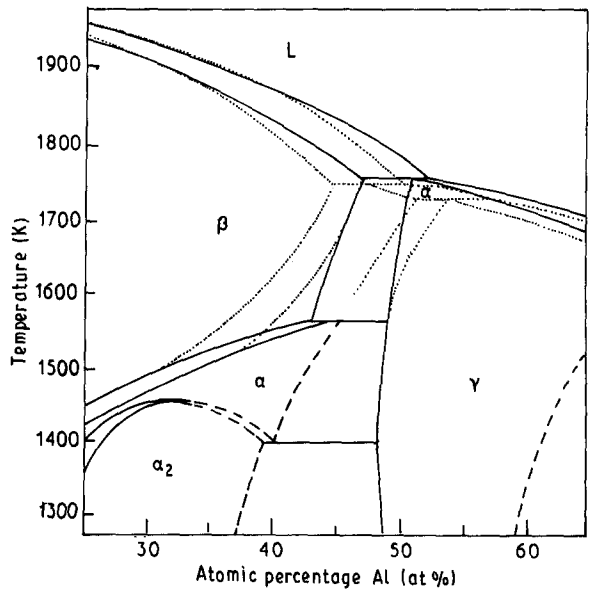

Figure 6 Part of the Ti–Al phase diagram as reported by Murray [9] (———) and McCullough [10] (– – –) -superimposed.

4.3. Hardness/structure relationships

Fig. 7 shows the hardness as a function of aluminium content, including a value for an alloy containing 36 at %Al [12]. The highest hardness, which corresponds to 43 at %Al, is associated with a structure which is predominantly ordered α_2. In the 50 and 55 at %Al alloys, there are increasing proportions of lamellar $\alpha_2 + \gamma$ structure, while at 60 at %Al, the structure is entirely single phase γ. The fine domain structure of α_2 is interpreted as a dominant strengthening mechanism. γ phase, although ordered, does not show domains and is of relatively low hardness. The $TiAl_3$ structure in the 80 at %Al alloy is also ordered, but showed no domains, and is of lower hardness (300Hv—Table 1) than α_2.

It is of interest to note that the hardness values reported [1] (Fig. 7) differ from the present results

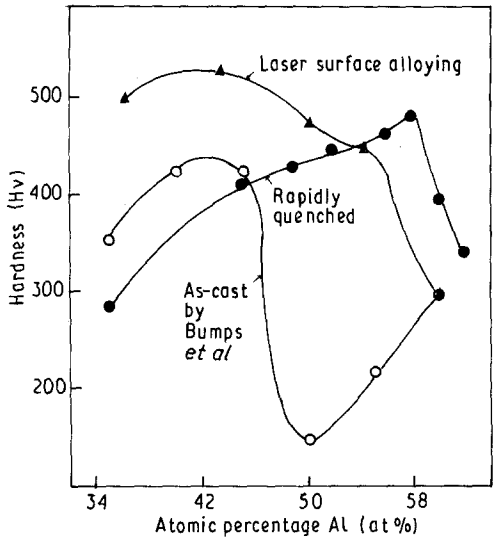

Figure 7 Variation of average hardness with average Al content for: (▲) laser surface Ti–Al alloyed zones; (●) rapidly quenched Ti–Al alloys [1]; (○) and as-cast Ti–Al alloys [12].

in that they show a progressive increase in hardness of rapidly quenched Ti–Al alloy in the range ~ 40–57 at %Al; the cooling rate employed was ~ 10^5–10^6 °C s^{-1} which is higher than in the present work and the structures were reported to consist of α_2 and γ.

The results of Bumps *et al.* [13] on as-cast alloys show a similar trend to the present results in the relevant composition range. However, the hardness levels are lower in the range where $\alpha_2 + \gamma$ structures exist. The higher values in the present work may be attributable to structural refinement (grain and domain sizes), and, possibly, the present alloys may have higher oxygen contents.

5. Conclusions

Optical, SEM, TEM, and STEM examinations have shown that by the use of CO_2 lasers and powder feed technique, rapidly solidified Ti–Al alloyed layers can be produced over a wide composition range. The phases present in the compositions 43–80 at %Al were: dendrites of α_2 and interdendritic regions consisting of $\alpha_2 + \gamma$ in the Ti–43 at %Al alloy; dendrites of either α_2 or $\alpha_2 + \gamma$ and interdendritic regions of γ in the Ti–50 at %Al alloy; dendrites of $\alpha_2 + \gamma$ and interdendritic γ in the Ti–55 at %Al alloy; single phase γ in the Ti–60 at %Al alloy, and $TiAl_3$ dendrites and Al solid solution in the interdendritic regions in the Ti–80 at %Al alloy. The microstructures of the Ti–50 at %Al and Ti–55 at %Al alloys are consistent with the occurrence of the peritectic reactions $L + \beta \rightarrow \alpha$ and $L + \alpha \rightarrow \gamma$ and not the reaction $L + \beta \rightarrow \gamma$.

Acknowledgements

Acknowledgements are made to the Ministry of Education of Iraq for the award of a scholarship to one of the authors (J. A.), to SERC for financial support, to H. M. Flower for helpful discussion, and also to Imperial Metal Industries Ltd for supplying titanium.

References

1. S. H. WHANG, D. VUJIC and Z. X. LI, in "Processing of Structural Materials by Rapid Solidification", edited by F. H. Froes and S. J. Savage (ASM, 1987) p. 191.
2. J. A. GRAVES, J. H. PEREPEZKO, C. H. WARD and F. H. FROES, *Scripta Metall* **21** (1987) 567.
3. J. A. GRAVES, L. A. BENDERSKY, J. H. PEREPEZKO and W. J. BOETTINGER, *Mater. Sci. Eng.* **98** (1988) 265.
4. E. L. HALL and S. C. HUANG, *Acta Metall.* **38** (1990) 539.
5. J. H. ABBOUD and D. R. F. WEST, *Mater. Sci. Technol.* **7** (1991) 353.
6. *Idem, ibid.* **7** (1991) 827.
7. J. BLACKBURN, in "The Science, Technology, and Applications of Titanium", edited by R. I. Jaffee and N. E. Promisel (Pergamon Press, 1970) p. 633.
8. P. DUWEZ and J. L. TAYLOR, *J. Metals, Trans. AIME*, **4** (1952) 70.
9. J. L. MURRAY, in "Binary Alloy Phase Diagrams", edited by T. B. Massalski (ASM, Metal Park, 1986) p. 173.
10. E. McCULLOUGH, J. J. VALENCIA, C. G. LEVI and R. MEHRABIAN, *Acta Metall.* **37** (1989) 1321.
11. H. W. KERR, J. CISSE and G. F. BOLLING, *ibid.* **22** (1974) 677.
12. J. H. ABBOUD, PhD thesis, University of London, London (1990).
13. E. S. BUMPS, H. D. KESSLER and M. HANSEN, *J. Metals, Trans. AIME* **194** (1952) 609.

Received 12 April
and accepted 1 May